frontiers | Frontiers in Coatings, Dyes and Interface Engineering

TYPE Original Research
PUBLISHED 27 May 2025
DOI 10.3389/frcdi.2025.1598207

OPEN ACCESS

EDITED BY
Arnaud Caron,
Liaoning Academy of Materials, China

REVIEWED BY
Alicja Krystyna Krella,
Polish Academy of Sciences, Poland
Hao Zhou,
Liaoning Academy of Materials, China

*CORRESPONDENCE
Q. Y. Li,
qingyang@jnu.edu.cn
D. Y. Li,
dongyang.li@ualberta.ca

†These authors have contributed equally to this work

RECEIVED 22 March 2025
ACCEPTED 12 May 2025
PUBLISHED 27 May 2025

CITATION
Xu Z, Diao G, Tang Y, Chen K, Lin K, He A, Fraser D, Li J, Chung R, Li QY and Li DY (2025) Effects of rare-earth element yttrium (Y) on the solid-particle erosion resistance of AlCrFeNi medium-entropy alloy at ambient and elevated temperatures.
Front. Coat. Dyes Interface Eng. 3:1598207.
doi: 10.3389/frcdi.2025.1598207

Effects of rare-earth element yttrium (Y) on the solid-particle erosion resistance of AlCrFeNi medium-entropy alloy at ambient and elevated temperatures

Zhen Xu[1†], Guijiang Diao[1†], Yunqing Tang[2], Keyang Chen[2], Kaifan Lin[1], Anqiang He[1], Doug Fraser[3], Jing Li[3], Rei Chung[4], Q. Y. Li[5]* and D. Y. Li[1]*

[1]Department of Chemical and Materials Engineering, University of Alberta, Edmonton, AB, Canada, [2]State Key Laboratory of Advanced Equipment and Technology for Metal Forming, Shandong University, Jinan, China, [3]Trimay Wear Plate Ltd., Edmonton, AB, Canada, [4]Suncor Energy Inc, Calgary, AB, Canada, [5]Institute of Advanced Wear & Corrosion Resistant and Functional Materials, Jinan University, Guangzhou, China

High-entropy alloys (HEAs) and medium-entropy alloys (MEAs) have demonstrated many superior properties, including high strength, toughness, and thermal stability. Among MEAs, AlCrFeNi has received considerable attention due to its well-balanced mechanical properties and cost-effectiveness, making it a promising candidate for industrial applications. It is known that rare-earth elements can effectively enhance the oxidation resistance of alloys containing passive elements. In this study, AlCrFeNi MEAs with Y additions (0.5, 1.0, and 1.5 wt.%) were fabricated by arc melting. Microstructures of fabricated samples and their mechanical properties and resistance to air-jet sand erosion were investigated at both room temperature (20°C) and elevated temperature (700°C). For the sake of comparison, a commercial nickel-based Waspaloy superalloy was also evaluated. At both room and elevated temperatures, the AlCrFeNi MEA demonstrated high superiority over the widely used nickel-based superalloy. The Y additions increased the hardness and yield strength of the MEA, leading to improved erosion resistance at room temperature, which was more obvious at elevated temperatures, largely benefiting from the improved resistance to accelerated oxidation at elevated temperatures. The obtained information highlighted the beneficial effects of the minor Y additions in enhancing both the mechanical performance and high-temperature durability of the AlCrFeNi MEA, which would help extend the application of the MEA to higher temperatures.

KEYWORDS

high-temperature erosion, AlCrFeNi medium-entropy alloy, yttrium addition, oxidation resistance, Ni-based superalloy

1 Introduction

High- and medium-entropy alloys (HEAs/MEAs) are multi-component alloys, which have garnered considerable interest since 2004 (George et al., 2019; Yeh, 2006). These alloys may exhibit combinations of many superior properties, including high strength and toughness, excellent wear resistance, superior corrosion resistance, and exceptional thermal stability (Zhang et al., 2014; Tsai and Yeh, 2014). Among MEAs, the cost-effective AlCrFeNi alloy, composed of four main elements in equiatomic proportions, has been extensively studied. This composition promotes the formation of a body-centered cubic (BCC) solid solution, which benefits its mechanical performance and wear resistance at room temperature (Xu et al., 2024a; Wu et al., 2023; Qiao and Zhu, 2022). At elevated temperatures, AlCrFeNi-based MEAs develop protective oxide layers on their surfaces due to the presence of passive elements such as Al and Cr, which oxidize to form dense and adherent Al_2O_3 and Cr_2O_3 scales, respectively (Chen et al., 2017; Shi et al., 2021).

The addition of rare-earth elements, particularly yttrium (Y), has been shown to be able to enhance both the mechanical properties and oxidation resistance of HEAs and MEAs (Zhou et al., 2025; Li et al., 2020; Ren et al., 2024). Zhou et al. (2025) investigated the influences of Y addition on the microstructure and mechanical properties of FCC $CoCr_{1.7}NiY_x$ (x = 0, 0.01, 0.02, 0.03, 0.04, and 0.1 at. %) MEAs. Results of the study revealed that a YNi_5 HCP phase precipitated in the $CoCr_{1.7}NiY_{0.01}$ alloy, and as Y content increased, the volume fraction of BCC and the HCP precipitates also grew. The phase transformations enhanced the strength and hardness of the $CoCr_{1.7}NiY_x$ alloys, with the largest improvement observed at 0.1 at. % Li et al. (2020) examined the effects of Y additions (0.1, 0.2, and 0.5 at. %) on the microstructure and properties of $FeCoNi_{1.5}CuB$ HEAs. The $FeCoNi_{1.5}CuBY_{0.2}$ sample demonstrated the highest compressive strength, yield strength, and maximum compression ratio, attributed to the combined effects of solid-solution strengthening, grain refinement, and dispersion strengthening. However, as Y content exceeded 0.2 at. %, the high-entropy alloy structure was disrupted, reducing the inhibition of boride growth and leading to deterioration in mechanical properties. Ren et al. (2024) studied the mechanical behavior and oxidation resistance of $(AlCoCrFeNi)_{100-x}Y_x$ (x = 0, 0.1, 0.5, and 1 at. %) HEAs. Their results showed that a small Y addition significantly enhanced oxidation resistance, with the Y-0.1 HEA demonstrating the best performance due to the formation of oxide pegs and the absence of interfacial defects. However, excessive Y led to the formation of (Y, Ni)-rich oxide intrusions, which negatively influenced the oxidation resistance.

It is well established that small amounts of rare-earth elements improve the adhesion of oxide films to metal substrate, but this benefit diminishes when Y content exceeds an optimal threshold. To better understand this phenomenon, Li and Li (2019) employed *ab initio* calculations to assess the role of Y in strengthening the adhesion of Al_2O_3 to an Al substrate. Their study demonstrated that an optimal Y concentration enhanced Al/Al_2O_3 interfacial bonding, while excessive Y weakened the system by disrupting the bonding between Y^{3+} ions and O^{2-} ions within the oxide layer. This study helps understand the mechanism behind and properly utilize the rare-earth element to obtain desirable properties.

The resistance of materials to sand erosion is influenced by multiple factors, including impingement angles, hardness and toughness of the material, and its ability to develop protective oxide layer (Bousser et al., 2014; Arabnejad et al., 2015; Chen and Li, 2003). High hardness enhances the resistance to sand particle penetration, while toughness aids in absorbing impact energy to reduce the probability of cracking. Erosion studies conducted under both ambient and elevated temperatures have demonstrated that HEAs retain their erosion resistance across a broad temperature range (Zhang et al., 2023; Nair et al., 2023; Zhang et al., 2021). Zhang et al. (2021) examined the solid particle erosion behavior of CoCrFeNiTi HEA coatings on a steel substrate at room temperature. The CoCrFeNiTi HEA coating exhibited an average microhardness of 568 HV0.2, approximately 2.5 times higher than that of the 304 stainless steel substrate (236 HV0.2). Their observations revealed that the HEA coating displayed considerably lower erosion rates than the substrate at both 30° and 60° impingement angles. The erosion mechanisms varied depending on the impingement angle: at oblique angles, material loss primarily occurred through ploughing and micro-cutting, whereas at vertical impact angles, crater formation became the dominant mechanism. These results indicate that HEAs and MEAs hold high potential for anti-wear applications involving sand erosion. However, the influence of Y addition on MEAs, particularly the cost-effective AlCrFeNi alloy, in terms of its mechanical properties and erosion resistance of HEAs and MEAs at elevated temperatures basically remains unexplored.

In this study, AlCrFeNi MEAs with different Y contents (0, 0.5, 1.0, and 1.5 wt.%) were synthesized using arc melting. Their microstructure, mechanical properties, and sand erosion resistance were systematically evaluated at both room temperature (20°C) and elevated temperature (700°C). A commercial nickel-based superalloy (Waspaloy) was included for the comparison purpose. Ni-based superalloys are well known for their superior mechanical strength, excellent thermal stability, and remarkable resistance to corrosion and oxidation at elevated temperatures (Gong et al., 2021; Stoyanov et al., 2018; McKamey et al., 2000). Their ability to sustain high strength and toughness while forming stable protective oxide layers makes the superalloys indispensable for high-temperature and high-stress applications (Hardy et al., 2020; Behera et al., 2023). Comparing the Y-modified AlCrFeNi MEAs with a commercial Ni-based superalloy provides a more perceptible assessment of their mechanical performance and erosion resistance under both ambient and high-temperature conditions.

2 Experimental details

High-purity Al, Cr, Fe, and Ni metal powders (>99%, >325 mesh, Sigma-Aldrich) along with yttrium metal powders (99.0%, −40 mesh, Aldrich Chemical) were utilized to synthesize AlCrFeNi+x wt.% Y (x = 0, 0.5, 1.0, and 1.5) samples through arc melting using a TA-200 arc melter (MRF). To prevent oxidation during the melting process, a protective argon atmosphere was maintained inside the arc chamber. Additionally, a commercial nickel-based superalloy (Waspaloy, McMaster-Carr) was prepared and tested for comparative analysis.

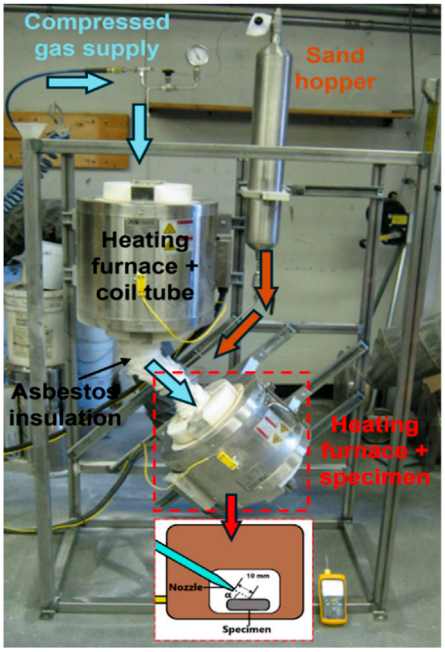

FIGURE 1
The high temperature air-jet sand erosion tester with superalloy components (up to 1,000°C).

FIGURE 2
SEM-SE images showing the morphology of SiO_2 sand particles.

Solid particle erosion tests were performed using a custom-built high-temperature air-jet sand erosion tester, as illustrated in Figure 1. The erodent material consisted of angular silica (SiO_2) sand particles (Sil 3, Sil Industrial Minerals, Canada), with a particle size range of 200–300 μm (Figure 2). The erosion setup had a tube nozzle with an inner diameter of 4.57 mm, positioned 10 mm from the sample surface. Sand particles were ejected at a velocity of 70 m/s under a constant air pressure of 276 kPa, impinged the sample at angles of 30° and 60° at both room temperature (20°C) and elevated temperature (700°C). Each erosion test utilized 1,500 g of sand, and sample weight loss caused by erosion was precisely measured using an analytical balance with a 0.1 mg resolution. The erosion rate, expressed as volume loss per unit sand weight (mm^3/g), was used to quantify material damage. Each reported value represents an average of at least three independent measurements.

A Rigaku XRD Ultima IV X-ray diffractometer (Japan) with Cu-Kα radiation was utilized to determine the phase composition of Y-reinforced AlCrFeNi samples within a 2θ scanning range of 20°–90° at a scanning speed of 3° min^{-1}. Microstructural analysis of the alloys and their eroded surfaces was conducted using a Zeiss EVO MA10 scanning electron microscope (SEM, Germany) equipped with an energy-dispersive X-ray spectroscopy (EDX) system.

Microhardness (HV5) measurements were performed at room temperature, 400°C, and 700°C using a high-temperature Vickers hardness testing system (HTV-PHS30, ARCHIMEDES, China) under an indent load of 5 kgf. Each reported hardness value represents the average of at least five measurements per sample. Compressive stress-strain curves were obtained from cylindrical specimens (Φ4 × 7.0 mm) using an electromechanical universal testing machine (TESTRESOURCES 313, USA) operated at a displacement rate of 0.3 mm/min.

To assess high-temperature oxidation behavior, isothermal oxidation tests were performed on ground samples at 750°C in air for 100 h using a F79300 tube furnace (Thermolyne, Barnstead, US). During the 100-hour isothermal oxidation test at 750°C, the samples were removed from the furnace at specific time intervals, cooled in air to room temperature, and then weighed using an analytical balance with a precision of 0.1 mg. This procedure was repeated at each time point to record the cumulative mass gain. The cooling process involved placing the samples on a ceramic plate in ambient air, allowing them to naturally cool to room temperature without forced convection. Once fully cooled, the samples were handled with clean tweezers to avoid contamination, and measurements were performed under consistent laboratory conditions to ensure accuracy.

3 Results and discussion

3.1 Microstructural characterization

The XRD patterns of AlCrFeNi + x wt.% Yttrium (x = 0, 0.5, 1.0 and 1.5) MEAs are shown in Figure 3a. The AlCrFeNi MEA exhibits a dual-phase BCC structure, consisting of a disordered BCC (A2) phase and an ordered BCC (B2) phase, with overlapped diffraction peaks observed at 44°, 64° and 82° (Xu et al., 2024b; Diao et al., 2024; Jiang et al., 2019). As illustrated in the enlarged XRD patterns (30°–50°) in Figure 3b, the diffraction peaks of the A2 and B2 phases shrift to higher angles with increasing Y content. This shift is attributed to changes in lattice parameters, primarily due to the incorporation of Y atoms, which have a larger atomic radius than the other constituent elements in the matrix (Long et al., 2023). Furthermore, diffraction peaks corresponding to a hexagonal YNi_5 phase in the AlCrFeNi + 1.5 wt.% Y alloy are observed at 32°, 36°, 39°, 42° and 43° (Du and Zhang, 1996; Khrussanova et al., 2000; Zhou et al., 2023). The hexagonal phase is identified to have a $CaCu_5$ type structure with a P6/mmm space group (Zhang et al., 2018).

The SEM backscattered electron (BSE) images of AlCrFeNi alloys with 0.5–1.5 wt.% Y additions are shown in Figure 4. Both the AlCrFeNi and AlCrFeNi + 0.5 wt.% Y alloy MEAs (Figures 4a,b)

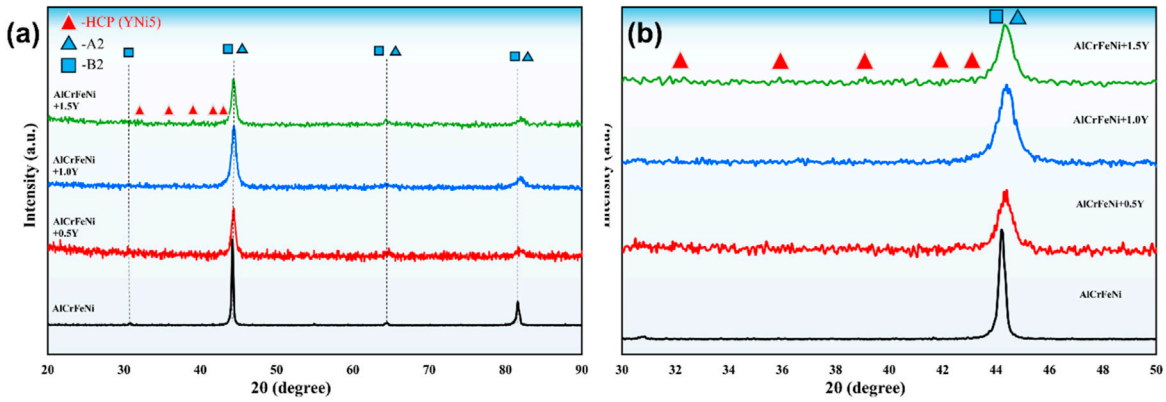

FIGURE 3
XRD patterns of the **(a)** AlCrFeNi+x wt.% Y MEAs (x = 0.5–1.5) and **(b)** enlarged XRD pattern at 30°–50°.

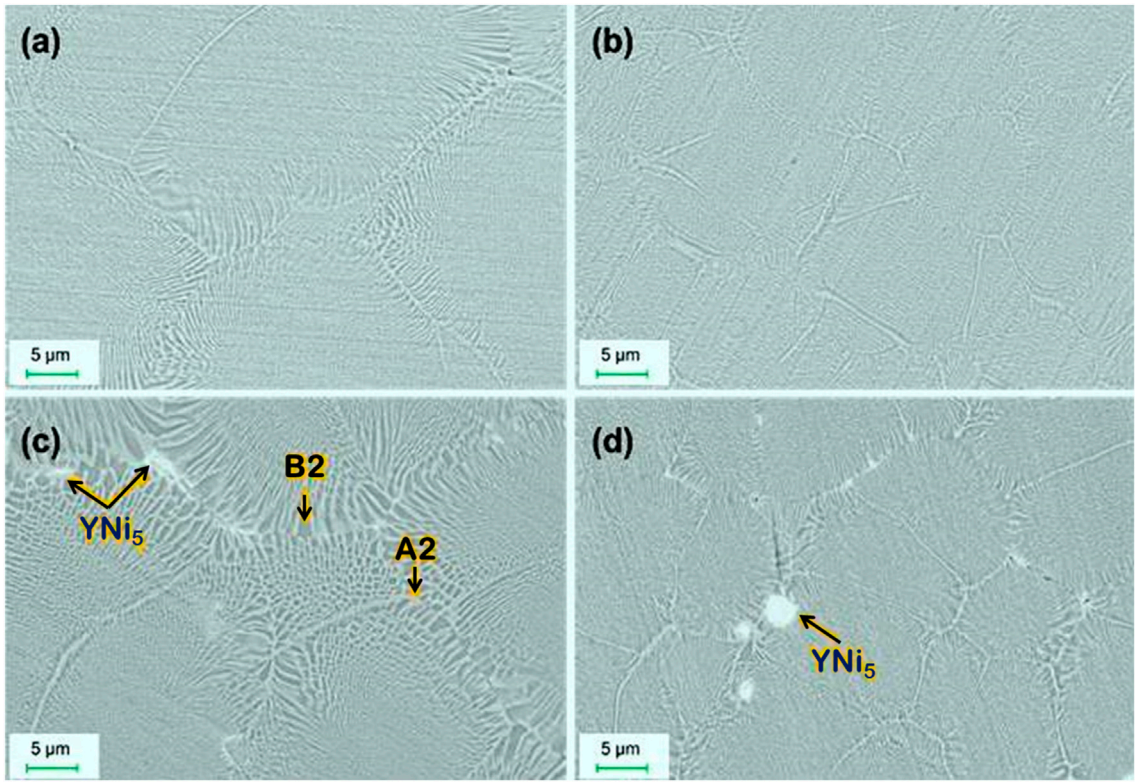

FIGURE 4
SEM-BSE images of microstructures: **(a)** AlCrFeNi MEA, **(b)** AlCrFeNi+0.5 wt.%Y, **(c)** AlCrFeNi+1.0 wt.%Y, **(d)** AlCrFeNi+1.5 wt.%Y.

exhibited a honeycomb-shaped microstructure, consisting of two distinct phases: the dark B2 phase and the lighter A2 phase, which align with the XRD analysis. In the AlCrFeNi + 0.5 wt.% Y alloy, a small amount of Y existed in the alloy matrix, leading to, more or less, some solid-solution strengthening effect on the matrix phase. As the Y content increased, an HCP phase began to precipitate from the matrix, with a progressive increase in the volume fraction of the precipitates in the AlCrFeNi + 1.0 wt.% Y and AlCrFeNi + 1.5 wt.% Y alloys (Figures 4c,d). The grain size and percentage of Y-rich precipitate fraction for AlCrFeNi and AlCrFeNi+ x%Y MEAs (x = 0.5–1.5) were analyzed using the Image-Pro Plus 6.0 (IPP 6.0) software based on the obtained SEM images. Results are listed in Table 1. The precipitate fraction (YNi_5) was observed to increase with Y content. As shown in Figures 4a,d, the average grain sizes of AlCrFeNi, AlCrFeNi + 0.5 wt.% Y, AlCrFeNi + 1.0 wt.% Y, and AlCrFeNi + 1.5 wt.% Y are approximately 15.0 μm, 8.0 μm, 12.0 μm, and 9.0 μm, respectively, confirming the grain refinement effect with increasing Y addition. This refinement effect is attributed to the

TABLE 1 Grain sizes and area fractions of the white YNi_5 precipitates for AlCrFeNi and AlCrFeNi+ x%Y MEAs (x = 0.5–1.5).

Alloys	Grain sizes/μm	Fractions of YNi_5
AlCrFeNi	15.0 ± 3.0	/
AlCrFeNi+0.5%Y	8.0 ± 2.0	/
AlCrFeNi+1.0%Y	12.0 ± 2.0	1.65%
AlCrFeNi+1.5%Y	9.0 ± 2.0	4.29%

TABLE 2 Chemical compositions (at.%) of original AlCrFeNi and AlCrFeNi+ x %Y MEAs (x = 0.5–1.5).

Alloys	Al	Fe	Cr	Ni	Y
AlCrFeNi	24.4 ± 0.6	25.2 ± 0.8	24.8 ± 0.9	25.6 ± 1.0	/
AlCrFeNi+0.5%Y	24.6 ± 0.5	24.8 ± 0.7	24.9 ± 1.0	25.4 ± 0.8	0.3 ± 0.1
AlCrFeNi+1.0%Y	24.8 ± 0.5	24.8 ± 0.9	25.2 ± 0.8	24.7 ± 0.9	0.5 ± 0.1
AlCrFeNi+1.5%Y	24.3 ± 0.7	25.0 ± 1.0	25.1 ± 1.1	24.9 ± 1.2	0.7 ± 0.2

presence of Y in the solid-solution matrix and its ability to promote the formation of precipitates (e.g., YNi_5), which act as barriers to grain boundary migration, thus effectively suppressing the grain growth (Li et al., 2022; Kim et al., 2023).

Chemical compositions (at.%) of original AlCrFeNi and AlCrFeNi+ x%Y MEAs (x = 0.5–1.5), determined from SEM-EDX, are given in Table 2. Figure 5 displays SEM-BSE images and corresponding EDX elemental maps of the AlCrFeNi + 1.5 wt.% Y alloy. The elemental distribution maps indicate that Al, Cr, Fe, and Ni are uniformly distributed throughout the alloy matrix. In contrast, Y exhibits localized enrichment, forming discrete white YNi_5 precipitates (Wu et al., 2021), which appear to be located more at grain boundaries in the present AlCrFeNi medium-entropy alloy.

3.2 Mechanical properties and sand-erosion behavior of the alloys

Vickers hardness values (HV5) of AlCrFeNi + x wt.% Y MEAs and the reference Waspaloy Ni-based superalloy were measured at room temperature and elevated temperatures (400°C and 700°C) to evaluate their mechanical strength and thermal stability. As illustrated in Figure 6, at room temperature, the hardness of AlCrFeNi + x wt.% Y MEAs increased with Y content up to 1.0 wt.% Y, reaching a maximum of 494 HV5. This enhancement is attributed to solid-solution strengthening and grain refinement (as observed in Figures 4a,d), which contribute to improved mechanical properties (Wu and Hwang, 2002; Qian et al., 2020). However, further Y addition beyond 1.0 wt.% resulted in a decline in hardness for AlCrFeNi + 1.5 wt.% Y. The decreased hardness could be ascribed to the formation of Y-rich intermetallics (e.g., YNi5), which is hard but brittle, and may act as stress concentrators and trigger cracking under the indentation load. The brittleness increases the probability of cracking, which can lower the resistance to local plastic deformation under the indenter during the hardness measurement, leading to a decrease in the apparent hardness.

Hong and Hsueh (2022) performed nanoindentation and Vickers indentation tests on Y-added CoCrNi MEAs and found that the hardening effects by both solid-solution and grain boundary had minimal contributions to the enhancement of hardness, while the formation of harder HCP precipitates showed the main contribution. Excessive Y content in alloys promotes the precipitation of hard yet brittle intermetallic compounds (e.g., YNi_5 HCP), leading to an increase in brittleness, which may weaken the overall hardness and facilitate cracking during deformation (Chen et al., 2022). In contrast, the commercial Waspaloy exhibited the lowest hardness (215 HV5) at room temperature among the tested alloys. However, it is widely recognized for its exceptional thermal stability, high strength, and oxidation resistance at temperatures up to 1,200°C (Wang et al., 2024), making the superalloy a suitable reference material when performing high-temperature sand erosion tests for the MEAs containing Y addition.

At elevated temperatures, all tested materials became more or less softer, compared to their states at room temperature. The AlCrFeNi + 1.0 wt.% Y alloy showed the highest hardness at 700°C (379 HV5). Both pure AlCrFeNi and Y-modified ones demonstrated higher thermal stability, maintaining their hardness effectively. For comparison, the percent decreases in hardness of AlCrFeNi, AlCrFeNi + 0.5 wt.%, AlCrFeNi + 1.0 wt.%, AlCrFeNi + 1.5 wt.% and the superalloy are 22.2%, 24.2%, 23.3%, 26.2%, and 31.2%, respectively. The superior thermo-mechanical stability of AlCrFeNi samples with and without Y is attributed to the inherent high-temperature hardness of the MEA and formed phases caused by the Y addition (Ramanarayanan et al., 1988). This combination contributes to high strength retention and benefits their resistance to the sand erosion at various temperatures. In contrast, the commercial Ni-based superalloy exhibited a relatively larger hardness reduction (31.2%) at 700°C.

Figure 7 presents the measured erosion rates of AlCrFeNi + x wt.% Y MEAs and Waspaloy Ni superalloy at room temperature (20°C) at impingement angles of 30° and 60°, respectively. At the impingement angle of 30° (Figure 7a), the erosion rates of AlCrFeNi + x wt.% Y MEAs initially declined with increasing Y content but rose again for the AlCrFeNi + 1.5 wt.% Y alloy. AlCrFeNi + 1.0 wt.% Y MEA showed the lowest erosion rate (8.83×10^{-3} mm^3/g), primarily due to its high hardness. This improved resistance resulted from precipitation strengthening, solid-solution strengthening, and grain boundary strengthening (El Garah et al., 2023; Guimarães et al., 2020). Compared to the Waspaloy superalloy, the AlCrFeNi + x wt.% Y MEAs exhibited superior erosion resistance, consistent with the hardness ranking shown in Figure 6. A similar trend was observed at a 60° impingement angle (Figure 7b), where Y addition slightly improved erosion resistance. Again, the AlCrFeNi + 1.0 wt.% Y alloy showed the lowest erosion rate, while the erosion rate of the sample with 1.5 wt.% Y increased slightly, likely due to reduced hardness from excessive Y content. The erosion rates of the samples at 60° showed a trend similar to that of hardness and values of erosion rate are marginally higher than those at 30°. Metallic materials are able to absorb more energy than ceramic materials to resist erosion (Xu et al., 2025). Toughness, estimated from the area under compressive stress-strain curves, reflects a material's ability to absorb energy and undergo plastic deformation without fracturing (Hertzberg et al., 2020; Li et al.,

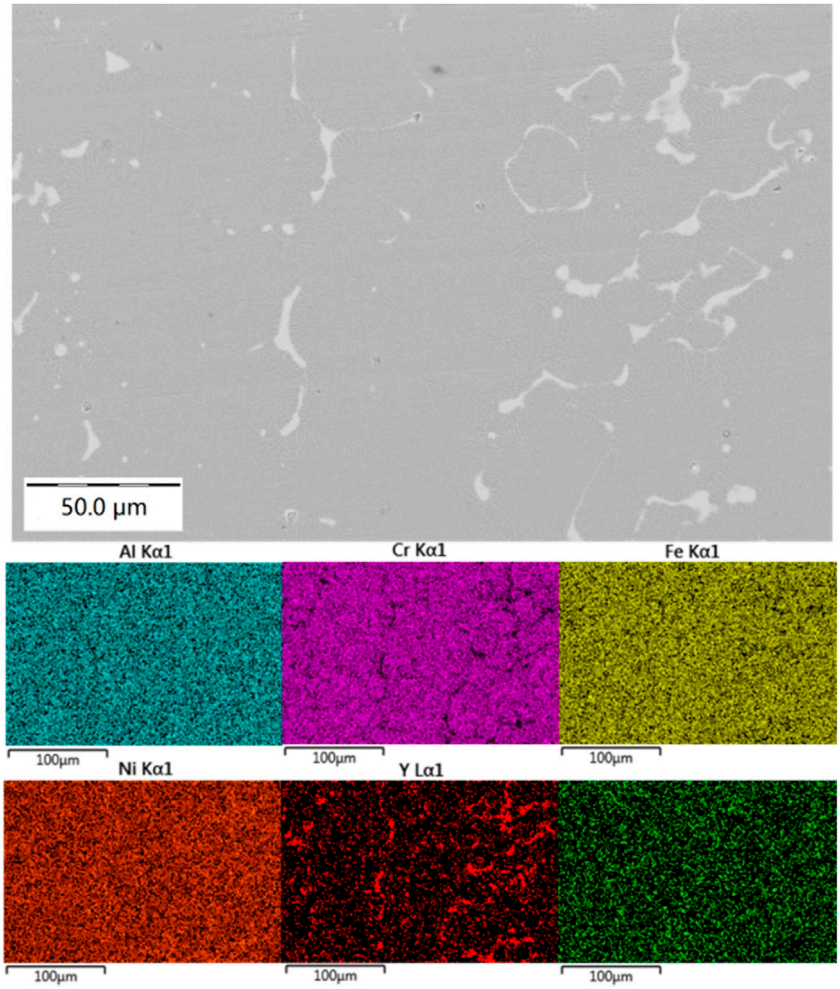

FIGURE 5
SEM-BSE images and corresponding EDX mapping of AlCrFeNi+1.5 wt.%Y showing the distribution of YNi5 precipitates.

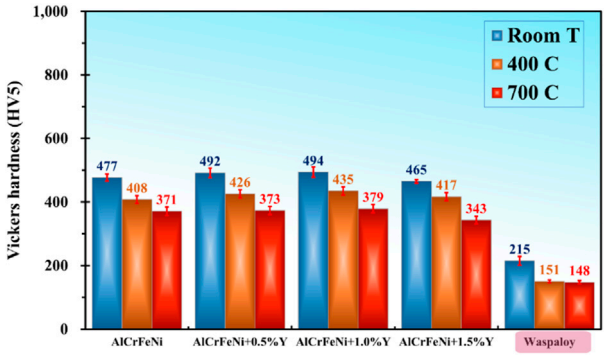

FIGURE 6
Hardness (HV5) of the Y-AlCrFeNi MEAs and Waspaloy at room temperature, 400°C and 700°C.

2018). Results of performed compressive tests for the materials under study are discussed later in this section to further evaluate mechanical properties of the material. It is worth noting that the influence of Y addition on erosion resistance at room temperature was relatively minor. Since the mechanical strength primarily determines the erosion resistance at ambient conditions. The Y addition is expected to be more beneficial at elevated temperatures sue to the fact that the rare-earth element can enhance the oxide scale.

To further investigate the erosion behavior, the eroded surfaces of selected alloys were examined. SEM-BSE images depicting their morphologies under different testing conditions are shown in Figures 8–12. Figure 8 illustrates the eroded surfaces of AlCrFeNi and AlCrFeNi + 1.0 wt.% Y MEAs eroded at a 30° impingement angle at room temperature. Distinct ploughing and micro-cutting features (marked by red arrows) were observed. The AlCrFeNi MEA (Figure 8a), with lower hardness, exhibited deeper furrows than the Y-added one (Figure 8b), confirming the improved erosion resistance of the latter. Figure 9 illustrates the eroded surfaces of samples impacted at 60°. Due to the higher impingement angle, greater vertical impact stress led to the formation of micro-indents, craters, and deformed platelets (highlighted by red arrows). Unlike the elongated micro-cuttings seen at a lower angle, the micro-indents at 60° were shorter but deeper. The vertical impact

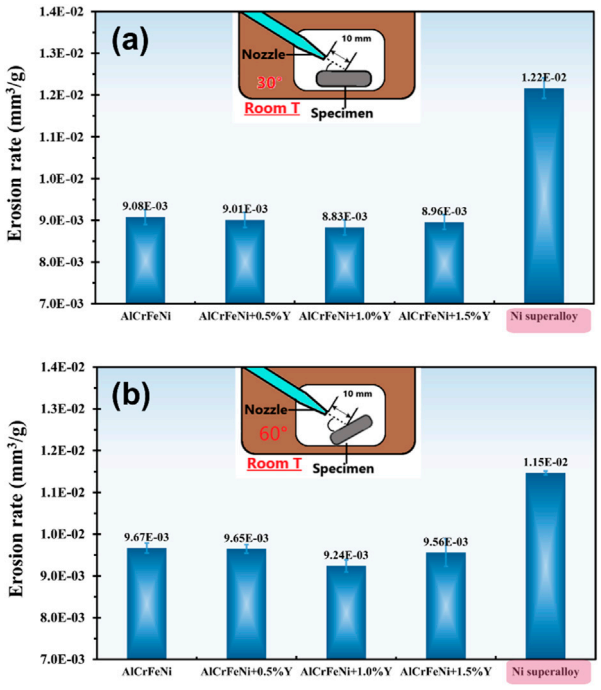

FIGURE 7
Erosion rates of HEAs and two reference alloys at room temperature with an impact angle of **(a)** 30°, and **(b)** 60°.

caused material displacement toward the indent edges, resulting in extruded lips. Continued material pile-up and deformation eventually led to fracture and erosion loss. Higher toughness plays a crucial role in mitigating erosion by absorbing more impact energy (Miyazaki, 2016).

Overall, the Y-added AlCrFeNi MEAs exhibited ductile erosion behavior, as indicated by the presence of grooves and ridges caused by ploughing and micro-cutting (Naveed et al., 2017). To evaluate the effect of Y addition on oxide scale formation, the chemical composition of the eroded surfaces was analyzed. EDX mapping of oxygen content (highlighted in green) is given in Figures 8, 9, and the surface compositions are summarized in Table 3. As illustrated, the surface of AlCrFeNi + 1.0 wt.% Y MEA showed more oxides than that of pure AlCrFeNi MEA, demonstrating Y's role in promoting protective oxide formation (Zhang et al., 2022). The oxides help enhance the erosion resistance by shielding the alloy surface from direct attack, as evidenced by the shallower and shorter furrows in the Y-containing MEA.

Figure 10 presents the erosion rates of the alloys eroded at 700°C, at impingement angles of 30° and 60°, respectively. The Y addition facilitates the formation of stable, protective oxides on the MEAs, benefiting their erosion resistance at elevated temperatures. As shown in Figure 10A, Y significantly increased the erosion resistance of AlCrFeNi MEA at 700°C at the impingement angle of 30°, with the AlCrFeNi + 1.0 wt.% Y MEA exhibiting the lowest erosion rate of 1.20×10^{-2} mm³/g. Similar to the trend observed at room temperature, harder samples demonstrated lower erosion rates. However, at higher temperatures, the effect of Y was more pronounced due to its beneficial role in oxide formation. A similar trend was observed at the impingement angle of 60° (Figure 10B). The erosion rates of AlCrFeNi + x wt.% Y MEAs decreased with increasing Y content, reaching a minimum of 1.19×10^{-2} mm³/g for the AlCrFeNi + 1.0 wt.% Y MEA. However, further increasing the Y content, the erosion rate slightly increased, likely due to reduced protectiveness of the oxide scale by excessive Y content and related issues (Radu and Li, 2008; Radu and Li, 2007).

In general, higher temperatures reduce yield strength and hardness of materials, making them less resistant to erosion under mechanical stresses (Blau, 2010). However, the multi-element HEAs/MEAs can decrease element diffusion due to their lattice distortion, which more or less hinders atomic diffusion, thus reducing the temperature-induced softening and phase separation (Xu et al., 2015; McCormack and Navrotsky, 2021). Additionally, the high-entropy (S) of HEAs/MEAs lowers Gibbs free energy (G = H–TS), contributing to the material stability at elevated temperatures, which increase the entropy. Besides, the rare-earth element, Y, is widely recognized to be effective in improving the oxidation resistance by forming a protective oxide scale, particularly in high-temperature environments. These factors help mitigate the adverse effects of temperature rise on mechanical strength, benefiting the resistance of Y-containing MEAs to erosion at elevated temperatures.

The eroded surfaces of AlCrFeNi and AlCrFeNi + 1.0 wt.%Y MEAs, tested at 700°C with 30° and 60° impingement angles, respectively, are shown in Figures 11, 12. Their surface morphologies resemble those observed at room temperature (Figures 8, 9) but the surface roughness increased significantly at 700°C. This can be attributed to the general reduction in mechanical strength at elevated temperatures. Additionally, the surfaces eroded at 700°C show greater plastic deformation than those at room temperature due to increased ductility, as evident when comparing Figures 11, 12 with Figures 8, 9.

In general, an increase in temperature led to higher erosion rates for most alloys due to thermal softening of the materials and enhanced plastic deformation under impact. However, for Y-containing AlCrFeNi MEAs, the increase in erosion rate at 700°C was relatively moderate, attributed to the ability of maintaining high-temperature strength and the formation of protective oxide films. Notably, AlCrFeNi + 1.0 wt.% Y showed the lowest increase in erosion rate, indicating superior high-temperature erosion resistance.

Figure 13 presents representative cross-sectional profiles of the eroded surfaces for AlCrFeNi and AlCrFeNi + 1.0 wt.% Y MEAs eroded at 60° impingement angle. Both qualitative and quantitative analyses of erosion scar width and depth are provided, along with 3D morphological profiles illustrating erosion intensity. At both testing temperatures, the AlCrFeNi + 1.0 wt.% Y MEA exhibited significantly lower erosion scar depth, compared to the pure AlCrFeNi MEA, aligning with the erosion rate trends observed in Figures 7, 10. However, the scar widths remained similar. As shown in Figures 13a,c, at room temperature, the erosion scar depth of the AlCrFeNi + 1.0 wt.% Y MEA (695 μm) was 12.6% lower than that of the pure AlCrFeNi MEA (795 μm). At 700°C, this reduction increased to 17.4% (Figures 13b,d), highlighting the increased effectiveness of Y addition in enhancing oxidation resistance at elevated temperatures.

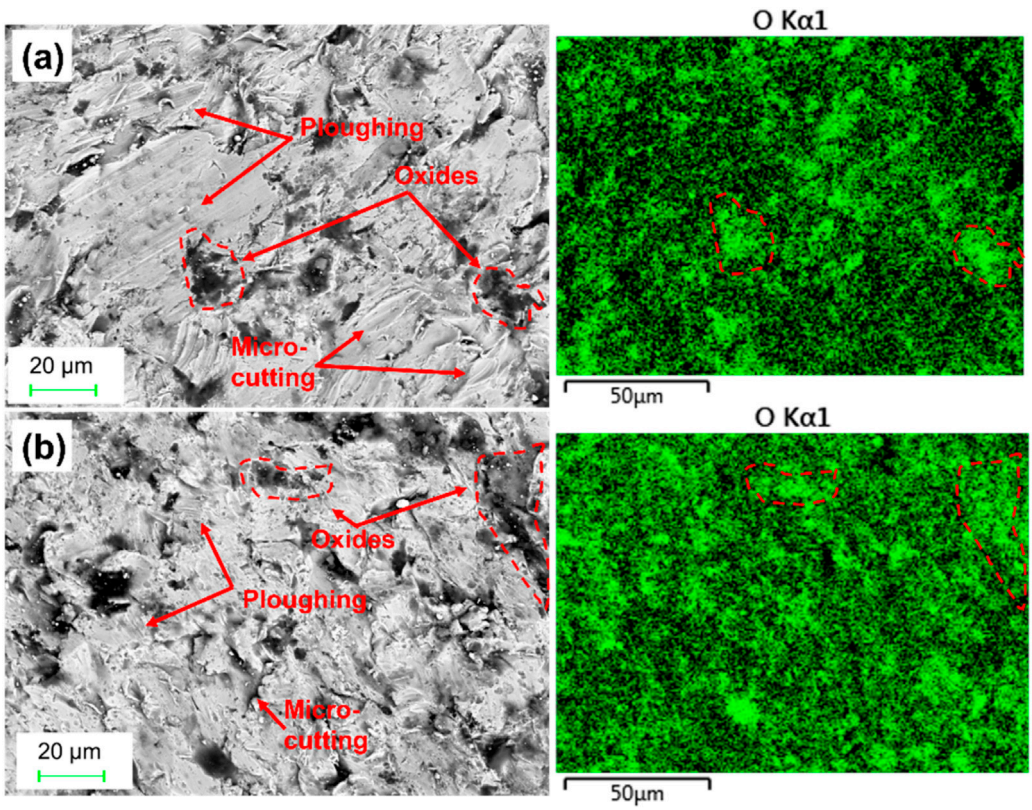

FIGURE 8
SEM-SE images and corresponding oxide content maps of the worn surfaces on **(a)** AlCrFeNi MEA and **(b)** AlCrFeNi+1.0 wt.%Y, respectively, eroded at the impingement angle of 30° at room temperature.

To evaluate the influence of Y addition on the mechanical properties of AlCrFeNi MEA, compressive tests were performed at room temperature. Figure 14 presents the compressive stress-strain curves of AlCrFeNi + x wt.% Y MEAs and the reference alloy (Waspaloy), with the corresponding mechanical property values listed in Table 4. As shown, adding a small amount of Y (≤1.0 wt.%) enhanced the compressive yield strength of the MEA at the expense of ductility. The AlCrFeNi + 1.0 wt.% Y MEA exhibited the highest yield strength (1,292 MPa), consistent with its highest hardness value. However, excessive Y (>1.0 wt.%) led to a decline in both strength and ductility in the AlCrFeNi + 1.5 wt.% Y MEA, attributed to the formation of brittle Y-rich intermetallic phases (Ren et al., 2022; Yi et al., 2021), which compromised toughness. The reduced ductility and toughness, as indicated by the area under the stress-strain curve, negatively influenced the benefit of Y addition to the erosion resistance of the MEAs.

An optimal Y content (below 1.5 wt.%) provided a balanced combination of strength and plasticity, which also led to the formation of a more protective oxide scale (Radu and Li, 2008; Radu and Li, 2007). In contrast, the Ni-based Waspaloy superalloy exhibited lower yield strength but significantly higher ductility, sustaining a strain of 71.2% without fracture. Although its superior plasticity and thermal stability may contribute to erosion resistance at elevated temperatures, its low hardness resulted in lower erosion resistance, compared with the AlCrFeNi MEAs, as illustrated in Figures 7, 10.

3.3 Isothermal high-temperature oxidation behavior of the Y-added MEAs

Since the MEAs under study contain passive elements such as Cr and Al, their erosion behavior is also influenced by oxidation and the formed oxide films on surface. The oxide films of passive elements are generally protective. Additionally, the rare-earth element Y can enhance the protectiveness of the oxide films (Radu and Li, 2008; Radu and Li, 2007).

To evaluate the performance of the oxide scale on the materials under the influence of Y, isothermal high-temperature oxidation tests were performed at 750°C for 100 h. Obtained mass gain curves are displayed in Figure 15. As shown, the oxidation-caused weight gain of the Y-added MEAs decreased with increasing Y content. After 100 h of oxidation, comparing AlCrFeNi and AlCrFeNi+1.5wt.%Y, the former has its weight gain about 60% more than that of the latter, indicating the effectiveness of the rare-earth Y in improving the oxidation resistance. For comparison, the commercial Ni-based Waspaloy displayed the largest weight gain. Since Waspaloy has a larger density than the MEA, the oxidation of Waspaloy could be similar to that of AlCrFeNi and is markedly faster than that on AlCrFeNi+1.5 wt.%Y MEA. During the initial oxidation stage (0–25 h), all samples experienced a relatively rapid mass increase due to the formation of oxide scales on the alloy surfaces. The oxidation rate was then slowed, resulting in a more stable state as the formation of adherent and protective oxide layers helped suppress continuous oxidation.

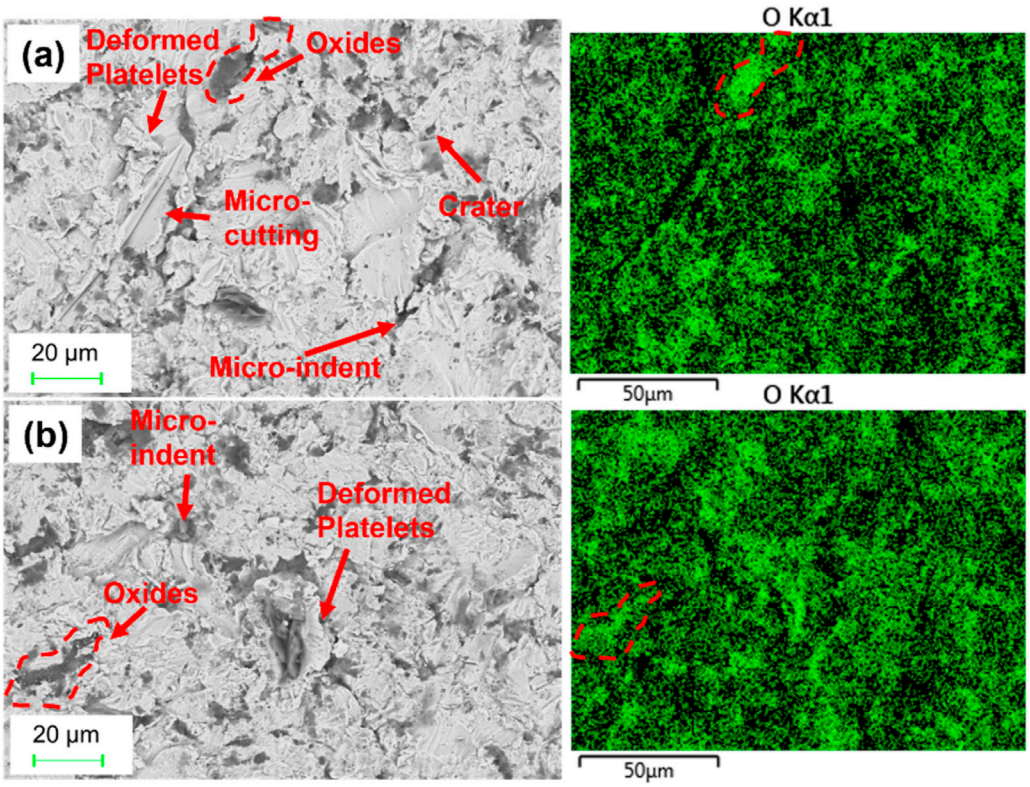

FIGURE 9
SEM-SE images and corresponding oxide content maps of the worn surfaces on **(a)** AlCrFeNi MEA and **(b)** AlCrFeNi+1.0 wt.%Y, respectively, eroded at the impingement angle of 60° at room temperature.

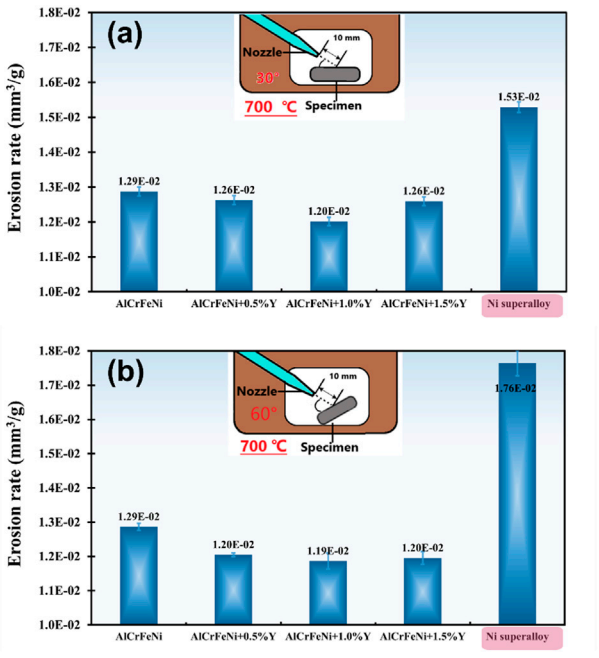

FIGURE 10
Erosion rates of MEAs and the superalloy as a reference alloy at 700°C with impingement angles of **(a)** 30°, and **(b)** 60°.

The cross-sectional characteristics and compositions of the oxide layers were examined using SEM-BSE imaging and EDX oxygen mapping (shown in green), as displayed in Figure 16. The protectiveness of an oxide scale depends on its thickness, adherence to the substrate, structural integrity and properties (Liu et al., 2021). Based on the obtained oxygen maps, the thickness of the oxide layers on the samples was analyzed. A relatively thick but structurally compromised oxide layer was observed on AlCrFeNi (Figure 16a), characterized by distinct cracks that negatively affected its protectiveness. In contrast, the oxide layers on AlCrFeNi + 1.0 wt.% Y and AlCrFeNi + 1.5 wt.% Y MEAs (Figures 16b,c) were significantly thinner, denser, and more uniform, without noticeable cracks or voids. Such compact oxide layers should effectively reduce continuous oxidation and shield the substrate by minimizing direct impingement from ejected sand particles. The oxide layer on the Ni-based Waspaloy alloy was loose and porous, with visible voids which reduced its protective capability against oxidation and erosion, which was consistent with the largest oxidation weight gain shown in Figure 15.

A strong oxide film helps resist erosion attacks. Although the thin oxide layer can be damaged during the erosion process, its dynamical and continuous growth/re-growth can more or less help mitigate sand-particle impingements on the MEAs. In other words, though the oxide film cannot completely block erosion, its continuous re-growth after being damaged provides a barrier to the erosion–caused attack to the metallic substrate. The yttrium can

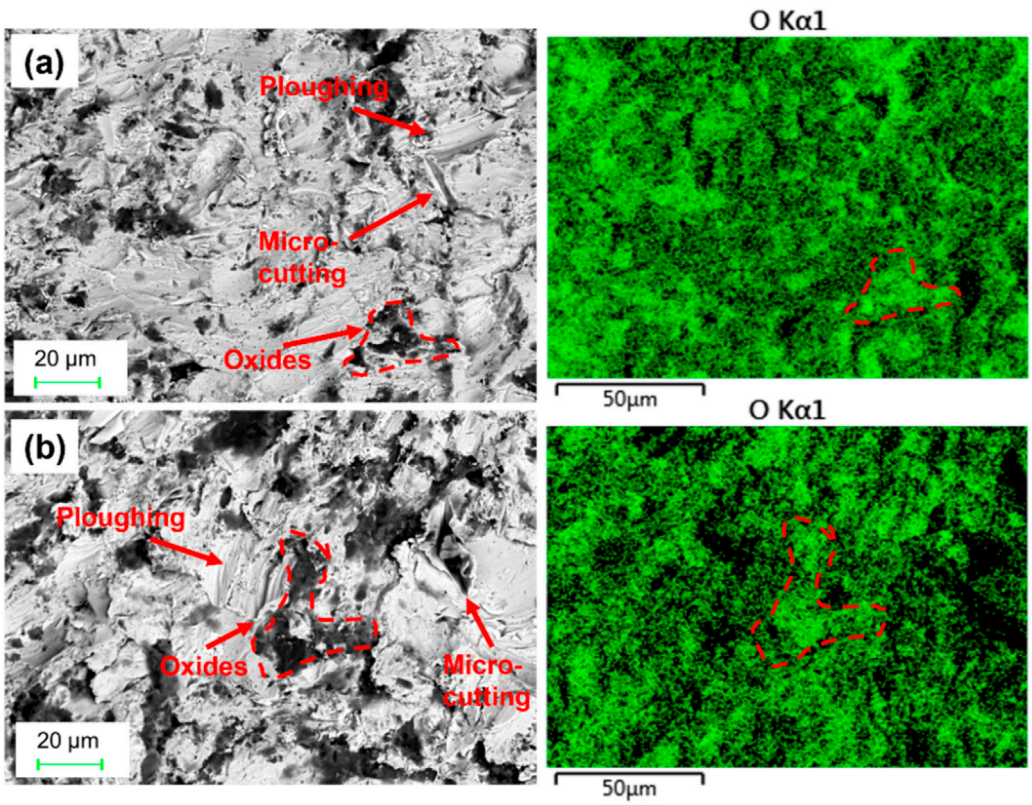

FIGURE 11
SEM-SE images and corresponding oxide content maps of the worn surface on **(a)** AlCrFeNi MEA and **(b)** AlCrFeNi+1.0 wt.%Y eroded at 700°C with an impingement angle of 30°.

TABLE 3 Chemical compositions (at.%) of eroded surfaces of AlCrFeNi and AlCrFeNi+ 1.0%Y alloys under different testing conditions.

Alloys	Conditions (Temperature/Impact angle)	Al	Fe	Cr	Ni	Y	O
AlCrFeNi	Room T/30°	18.3	20.5	20.3	20.0	/	20.9
	Room T/60°	18.5	17.6	17.8	17.3	/	28.7
	700°C/30°	18.0	18.3	18.7	18.4	/	26.6
	700°C/60°	15.5	15.4	14.6	13.9	/	40.6
AlCrFeNi+1.0%Y	Room T/30°	20.4	18.9	19.2	18.9	0.5	22.1
	Room T/60°	17.1	16.9	17.0	16.7	0.6	31.7
	700°C/30°	16.2	17.8	17.7	17.6	0.5	30.2
	700°C/60°	14.7	13.7	13.6	13.0	0.6	44.4

cause inward growth of oxide scale, which reduces the defects at the oxide-substrate interface and inside the oxide scale as well, thus further improving the durability of the oxide scale (Li and Li, 2019; Radu and Li, 2008; Radu and Li, 2007).

Yttrium (Y) is classified as a reactive element (RE) in oxidation studies, playing a crucial role in formation and growth of oxide scale (Migas et al., 2022). Research has shown that an optimal Y content in alloy matrix enhances the oxidation resistance by improving the adherence of Cr-rich and Al-rich oxide scales (Rovere et al., 2008). This improved adherence for the substrate is attributed to inward growth of oxide caused by Y, which suppresses void formation and mitigates interface degradation (Radu and Li, 2008; Whittle and Stringer, 1980). Studies on Fe-Cr-Al-Y alloys indicate that the Y incorporation results in more compact and adherent Al_2O_3 scales, significantly enhancing oxidation resistance (Kima et al., 2021). Similarly, in Fe-Cr-Y and Ni-Cr-Y alloys, Y promotes selective Cr oxidation, facilitating the formation of continuous Cr_2O_3 layers (Angeliu and Was, 1993). However, excessive Y can lead to the formation of brittle Y-rich phases (as observed in Figures 4, 5), reducing ductility. Besides, high Y concentrations may cause grain

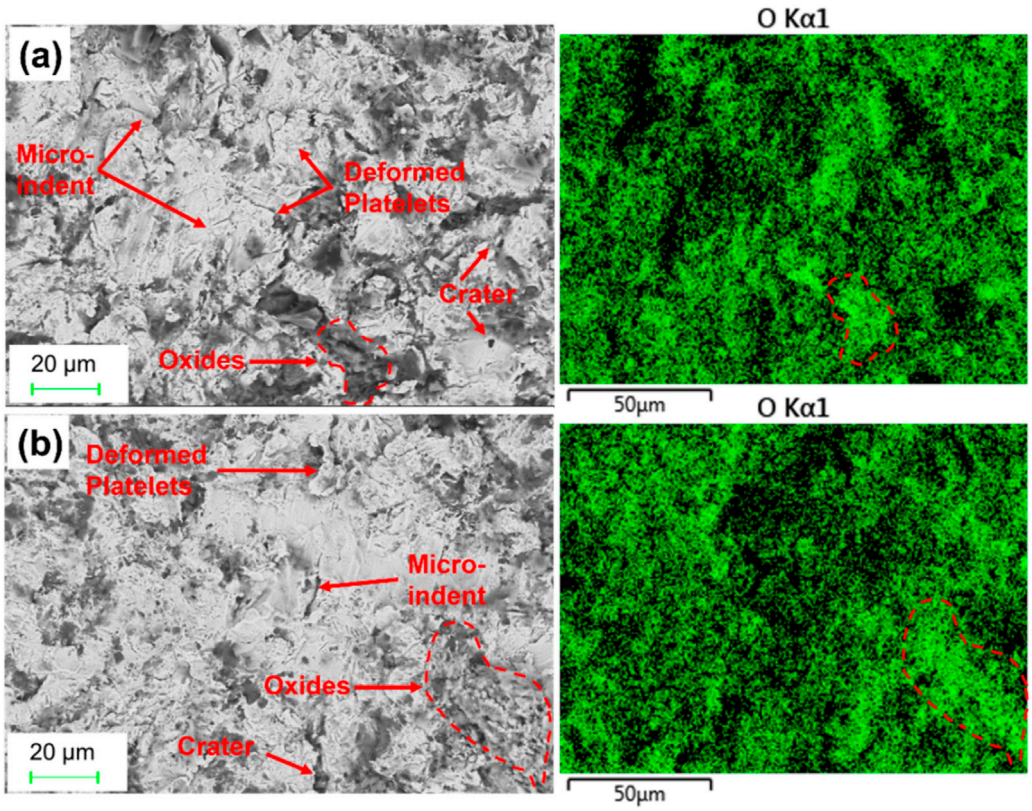

FIGURE 12
SEM-SE images and corresponding oxide content maps of the worn surface of **(a)** AlCrFeNi MEA, **(b)** AlCrFeNi+1.0 wt.% Y under the impact angle of 60° at 700°C.

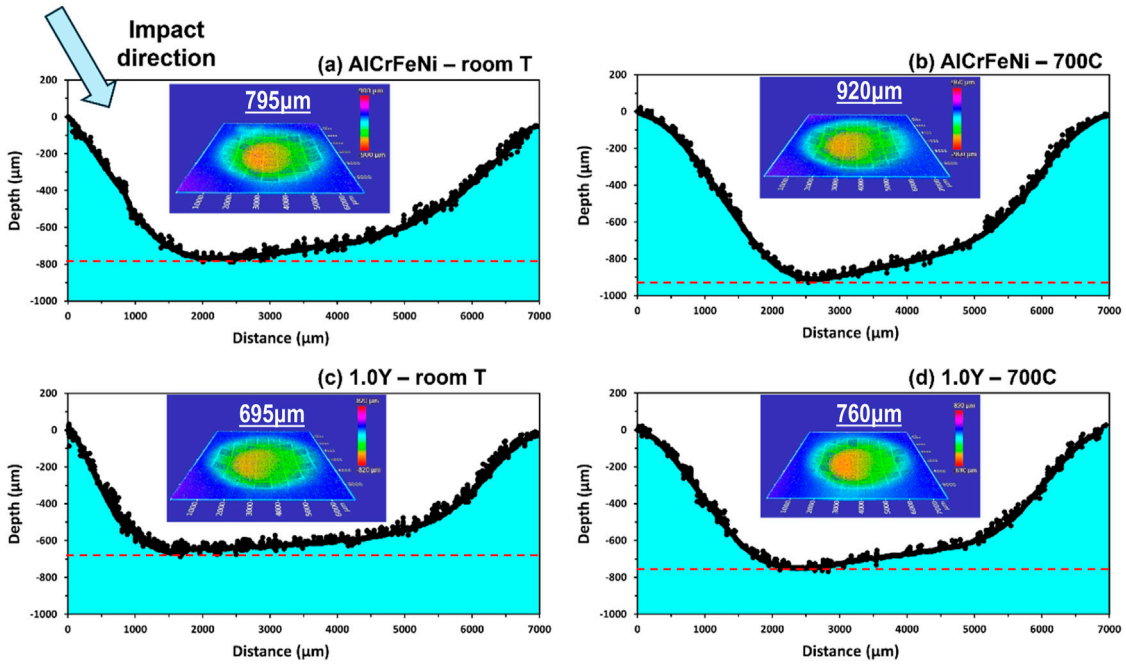

FIGURE 13
Eroded surface cross-sectional profiles of AlCrFeNi and AlCrFeNi+1.0%Y MEAs after sand erosion tests with an impingement angle of 60° at **(a)** and **(c)** room temperature, and **(b)** and **(d)** 700°C, respectively. The inserted graphs show corresponding 3D morphology of the eroded surfaces.

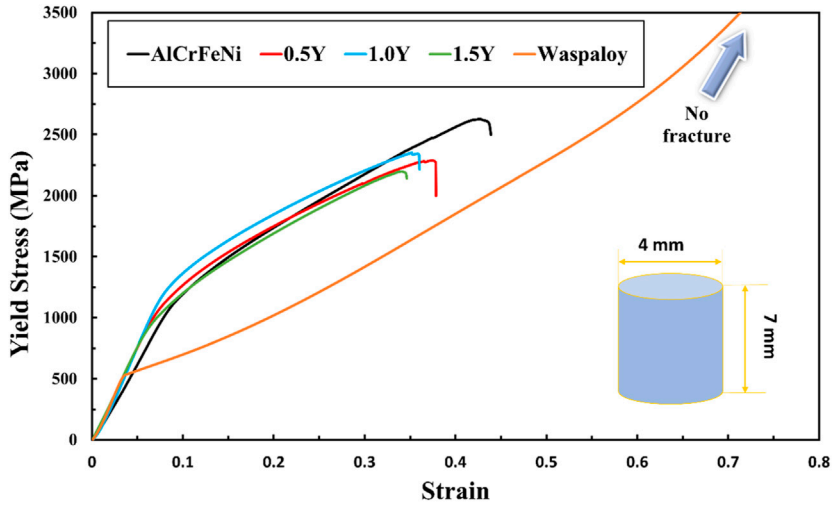

FIGURE 14
Compressive stress-strain curves of the MEAs and the superalloy.

TABLE 4 The compressive properties of the alloys at room temperature.

Alloy	Yield stress (0.2% offset, MPa)	Peak stress (MPa)	Failure strain (%)
AlCrFeNi AlCrFeNi+0.5 wt.%Y	1,143 1,184	2,627 2,288	43.7 37.9
AlCrFeNi+1.0 wt.%Y	1,292	2,338	36.0
AlCrFeNi+1.5 wt.%Y	1,170	2,196	34.6
Waspaloy Ni alloy	539	>3,493	>71.2

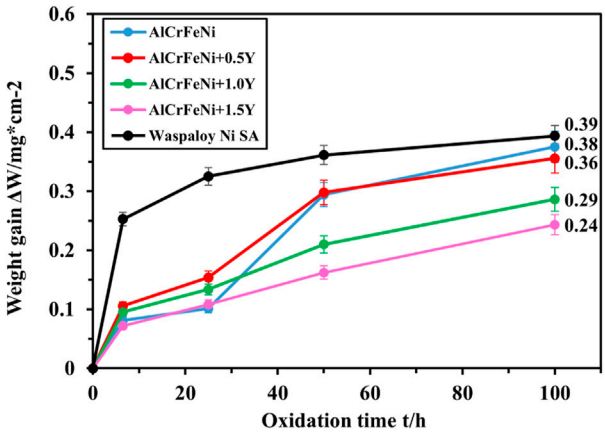

FIGURE 15
Oxidation kinetic curves of the Y-added AlCrFeNi MEAs and Waspaloy alloy oxidized at 750°C for 100 h in air.

boundary segregation and the development of porous oxides, adversely affecting mechanical properties and oxidation resistance (Li and Li, 2019; Radu and Li, 2007; Kindelmann et al., 2021).

In summary, Y addition in the AlCrFeNi MEA enhances the formation of a protective oxide layer during isothermal oxidation tests. However, an excessive Y content (>1.5 wt.%) may influence the oxide layer integrity. Therefore, AlCrFeNi MEAs with optimized Y additions achieve an optimal protective oxide film or scale, making them well-suited for high-temperature applications where conventional materials may fall short (Kuang et al., 2024).

Wear in aggressive environments is a complicated process. Significant efforts have been made to improve conventional wear-resistant materials using different approaches (Tang and Li, 2021; He et al., 2014; Ye et al., 1999; Li, 2000; Budinski and Budinski, 2021; Catalin et al., 2021). The non-conventional multi-element alloys, the medium- and high-entropy alloys, provide more opportunities to obtain superior tribological properties over conventional alloys. This study demonstrated that the AlCrFeNi medium-entropy alloy exhibits markedly superior erosion resistance than a nickel-based superalloy, and in particular, highlighted the beneficial effects of controlled Y additions in enhancing both the mechanical performance and high-temperature durability. The obtained information would help extend and speed up the applications of medium- and high-entropy alloys to those at elevated temperatures.

4 Conclusion

This article reports a study on effects of rare-earth element, yttrium, on microstructure, mechanical properties, and solid-particle erosion resistance of AlCrFeNi medium-entropy alloy

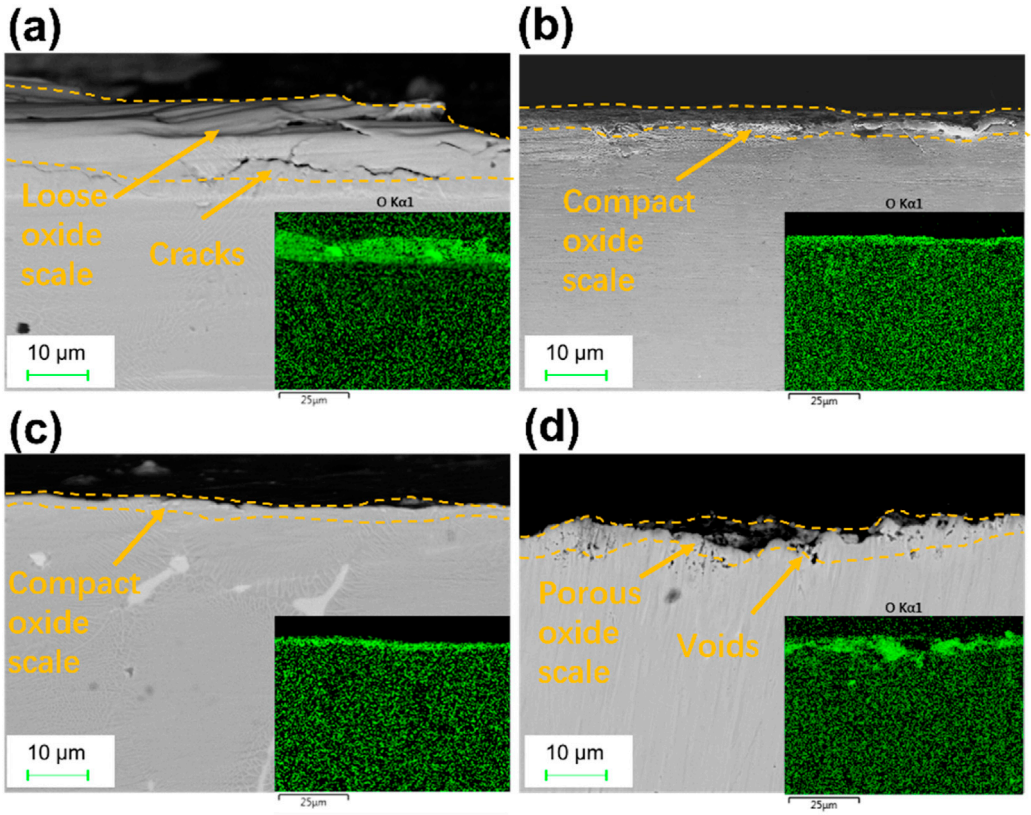

FIGURE 16
SEM-BSE images showing the cross-sectional characterizations of the eroded subsurface and corresponding EDX mapping of oxygen content after isothermal oxidation at 750°C for 100 h. **(a)** AlCrFeNi. **(b)** AlCrFeNi+1.0%Y. **(c)** AlCrFeNi+1.5%Y. **(d)** Ni Waspaloy.

(MEA) at both ambient and elevated (700°C) temperatures. The main findings are summarized as follows:

(1) AlCrFeNi MEAs with different Y contents (0, 0.5, 1.0, and 1.5 wt.%) were synthesized via arc melting. The base AlCrFeNi MEA consisted of an ordered Al-Ni-rich BCC (B2) phase and a disordered Cr-Fe-rich BCC (A2) phase. In the AlCrFeNi+1.5 wt.%Y MEA, YNi_5 precipitates having an HCP structure were also observed.

(2) The Y addition showed effects of solid-solution strengthening and grain boundary strengthening for the AlCrFeNi MEA. The AlCrFeNi+1.0wt.%Y alloy exhibited the highest hardness at both 20°C and 700°C. Compressive tests revealed that Y addition increased the yield strength of the MEA at the cost of ductility. The AlCrFeNi+1.0wt.%Y alloy achieved the best balance between strength and ductility. However, excessive Y (>1.0 wt.%) led to the formation of brittle the Y-rich intermetallic phase (YNi5), which decreased both strength and ductility in the AlCrFeNi + 1.5 wt.% Y MEA.

(3) The AlCrFeNi MEAs showed excellent erosion resistance at both room temperature and elevated temperature (700°C), compared with the Ni-based superalloy. Y addition increased the erosion resistance of AlCrFeNi MEAs particularly at the elevated temperature. The AlCrFeNi+1.0 wt.%Y alloy exhibited the lowest erosion rates at both ambient and elevated (700°C) temperatures, and the improvement is considerably larger than the room-temperature performance. This enhancement at the elevated temperature was attributed to the formation of a dense, adherent and protective oxide layer. In contrast, the oxide layers on pure AlCrFeNi and Ni-based superalloy samples were loose and porous, with visible cracks and voids, leading to reduced resistance to oxidation and high-T erosion.

(4) The Y-added AlCrFeNi MEAs demonstrated superior performance than commercial Ni-based superalloys at both ambient and elevated temperatures, demonstrating the potential of the AlCrFeNi MEAs with rare-earth minor Y addition for applications in high-temperature environments where conventional materials may fail.

Data availability statement

The raw data supporting the conclusions of this article will be made available by the authors, without undue reservation.

Author contributions

ZX: Conceptualization, Methodology, Writing – original draft, Investigation, Formal Analysis, Validation, Data curation. GD: Methodology, Validation, Formal Analysis, Conceptualization,

Writing – review and editing. YT: Writing – review and editing, Resources, Validation, Conceptualization, Methodology. KC: Resources, Validation, Writing – review and editing, Methodology. KL: Conceptualization, Validation, Writing – review and editing, Methodology. AH: Conceptualization, Writing – review and editing, Validation, Methodology, Formal Analysis. DF: Funding acquisition, Methodology, Writing – review and editing, Resources, Validation, Conceptualization. JL: Methodology, Writing – review and editing, Conceptualization, Resources, Validation. RC: Writing – review and editing, Methodology, Conceptualization, Validation, Resources. QL: Resources, Writing – review and editing, Funding acquisition, Validation, Methodology, Conceptualization. DL: Resources, Supervision, Funding acquisition, Formal Analysis, Writing – review and editing, Validation, Conceptualization, Methodology, Project administration.

Funding

The author(s) declare that financial support was received for the research and/or publication of this article. The authors are grateful for financial support from Natural Science and Engineering Research Council of Canada (NSERC AMA ALLRP 567506-21 Li), NSERC-NRCan (ALLRP 586454 – 23), Trimay and Mitacs (MI MA IT29134 Kumar/Xu/Li).

Conflict of interest

Authors DF and JL were employed by the company Trimay Wear Plate Ltd. Author RC was employed by the company Suncor Energy Inc.

The remaining authors declare that the research was conducted in the absence of any commercial or financial relationships that could be construed as a potential conflict of interest.

The author(s) declared that they were an editorial board member of Frontiers, at the time of submission. This had no impact on the peer review process and the final decision.

Generative AI statement

The author(s) declare that no Generative AI was used in the creation of this manuscript.

Publisher's note

References

Angeliu, T. M., and Was, G. S. (1993). The effect of chromium, carbon, and yttrium on the oxidation of nickel-base alloys in high temperature water. *J. Electrochem. Soc.* 140 (7), 1877–1883. doi:10.1149/1.2220732

Arabnejad, H., Mansouri, A., Shirazi, S. A., and McLaury, B. S. (2015). Development of mechanistic erosion equation for solid particles. *Wear* 332-333, 1044–1050. doi:10.1016/j.wear.2015.01.031

Behera, A., Sahoo, A. K., and Mahapatra, S. S. (2023). Application of Ni-based superalloy in aero turbine blade: a review. *Proc. Institution Mech. Eng. Part E J. Process Mech. Eng.*, 09544089231219104. doi:10.1177/09544089231219104

Blau, P. J. (2010). Elevated-temperature tribology of metallic materials. *Tribol. Int.* 43 (7), 1203–1208. doi:10.1016/j.triboint.2010.01.003

Bousser, E., Martinu, L., and Klemberg-Sapieha, J. E. (2014). Solid particle erosion mechanisms of protective coatings for aerospace applications. *Surf. Coatings Technol.* 257, 165–181. doi:10.1016/j.surfcoat.2014.08.037

Budinski, K. G., and Budinski, S. T. (2021). "Tribomaterials: properties and selection of materials for friction," in *Wear, and erosion applications*. Materials Park, OH, USA: ASM International.

Catalin, I. P., Aherwar, A., and Gorb, S. (2021). *Tribology and surface engineering for industrial applications* (Boca Raton, FL, USA: CRC Press).

Chen, Q., and Li, D. Y. (2003). Computer simulation of solid particle erosion. *Wear* 254 (3-4), 203–210. doi:10.1016/s0043-1648(03)00006-1

Chen, X., Sui, Y., Qi, J., He, Y., Wei, F., Meng, Q., et al. (2017). Microstructure of Al1.3CrFeNi eutectic high entropy alloy and oxidation behavior at 1000°C. *J. Mater. Res.* 32 (11), 2109–2116. doi:10.1557/jmr.2017.10

Chen, Y., Zhu, Z., and Zhou, J. (2022). Study on the strengthening mechanism of rare earth yttrium on magnesium alloys. *Mater. Sci. Eng. A* 850, 143513. doi:10.1016/j.msea.2022.143513

Diao, G., Wu, M., Xu, Z., Li, Q. Y., and Li, D. (2024). Manipulating A2/B2 microstructure via adjusting Al/Ni ratio in cost-effective Fe-based AlNiFeCr alloys for controllable strength-plasticity combination. *Mater. Charact.* 210, 113845. doi:10.1016/j.matchar.2024.113845

Du, Z., and Zhang, W. (1996). Thermodynamic assessment of the Ni-Y system. *J. Alloys Compd.* 245, 164–167. doi:10.1016/s0925-8388(96)02436-x

El Garah, M., Patout, L., Bouissil, A., Charai, A., and Sanchette, F. (2023). The effect of yttrium addition on microstructure and mechanical properties of refractory TiTaZrHfW high-entropy films. *Coatings* 13 (8), 1380. doi:10.3390/coatings13081380

George, E. P., Raabe, D., and Ritchie, R. O. (2019). High-entropy alloys. *Nat. Rev. Mater.* 4 515–534. doi:10.1038/s41578-019-0121-4

Gong, Z. H., Ma, Y. Y., Bao, H. S., and Yang, G. (2021). Effect of W on formation and properties of precipitates in Ni-based superalloys. *J. Iron Steel Res. Int.* 28, 910–919. doi:10.1007/s42243-021-00562-w

Guimarães, A. V., da Silveira, R. M. S., de Almeida, L. H., Araujo, L. S., Farina, A. B., and François Dille, J. A. (2020). Influence of yttrium addition on the microstructural evolution and mechanical properties of superalloy 718. *Mater. Sci. Eng. A* 776, 139023. doi:10.1016/j.msea.2020.139023

Hardy, M. C., Detrois, M., McDevitt, E. T., Argyrakis, C., Saraf, V., Jablonski, P. D., et al. (2020). Solving recent challenges for wrought Ni-base superalloys. *Metallurgical Mater. Trans. A* 51, 2626–2650. doi:10.1007/s11661-020-05773-6

He, H.-Bo, Han, W.-Q., Li, H. Y., Li, D. Y., Yang, J., Gu, T., et al. (2014). Effect of deep cryogenic treatment on machinability and wear mechanism of TiAlN coated tools during dry turning. *Int. J. Precis. Eng. Manuf.* 15, 655–660. doi:10.1007/s12541-014-0384-z

Hertzberg, R. W., Vinci, R. P., and Hertzberg, J. L. (2020). *Deformation and fracture mechanics of engineering materials*. John Wiley and Sons.

Hong, X., and Hsueh, C. H. (2022). Effects of yttrium addition on microstructures and mechanical properties of CoCrNi medium entropy alloy. *Intermetallics* 140, 107405. doi:10.1016/j.intermet.2021.107405

Jiang, Z., Chen, W., Xia, Z., Xiong, W., and Fu, Z. (2019). Influence of synthesis method on microstructure and mechanical behavior of Co-free AlCrFeNi medium-entropy alloy. *Intermetallics* 108, 45–54. doi:10.1016/j.intermet.2019.02.006

Khrussanova, M., Bobet, J. L., Terzieva, M., Chevalier, B., Radev, D., Peshev, P., et al. (2000). Hydrogen storage characteristics of magnesium mechanically alloyed with YNi5− xAlx (x= 0, 1 and 3) intermetallics. *J. alloys Compd.* 307 (1-2), 283–289. doi:10.1016/s0925-8388(00)00842-2

Kim, S., Lee, C. H., Kim, T., Jang, J. H., Moon, J., Falaakh, D. F., et al. (2023). Effects of yttrium on the oxidation behavior of Fe13Cr6AlY alloys under 1200°C steam. *J. Alloys Compd.* 960, 170642. doi:10.1016/j.jallcom.2023.170642

Kima, T., Kimb, S., Yooa, S. C., Hama, J., Leea, Y., Younga, S. I., et al. (2021). Corrosion behavior of Fe-Cr-Al alloys with yttrium addition on 360°C simulated pressurized water chemistry condition.

Kindelmann, M., Ran, K., Rheinheimer, W., Morita, K., Mayer, J., Bram, M., et al. (2021). Segregation-controlled densification and grain growth in rare earth-doped Y2O3. *J. Am. Ceram. Soc.* 104 (10), 4946–4959. doi:10.1111/jace.17907

Kuang, J., Wang, Q., Jia, Z., Yi, G., Sun, B., Yang, Y., et al. (2024). Ablation-resistant yttrium-modified high-entropy refractory metal silicide (NbMoTaW) Si2 coating for oxidizing environments up to 2100°C. *Mater. Today* 80, 156–166. doi:10.1016/j.mattod.2024.08.012

Li, D. Y. (2000). Development of novel wear-resistant materials: TiNi-based pseudoelastic tribomaterials. *Mater. and Des.* 21, 551–555. doi:10.1016/s0261-3069(00)00015-7

Li, G. R., Liu, M., Wang, H. M., Zhang, D., Tang, F., Wang, C. W., et al. (2020). Effect of the rare earth element yttrium on the structure and properties of boron-containing high-entropy alloy. *Jom* 72, 2332–2339. doi:10.1007/s11837-020-04059-x

Li, L., and Li, D. Y. (2019). A computational study on the effect of minor yttrium on the interfacial adherence of Al oxide film to aluminum substrate. *J. Phys. Condens. Matter* 31 (29), 295003. doi:10.1088/1361-648x/ab1864

Li, M., Xie, J., Gao, W., Zhan, Z., and Li, Z. (2022). Effect of yttrium on the oxidation resistance and areaspecific resistance of MnCo2O4 coating. *Surf. Coatings Technol.* 444, 128655. doi:10.1016/j.surfcoat.2022.128655

Li, W., Liaw, P. K., and Gao, Y. (2018). Fracture resistance of high entropy alloys: a review. *Intermetallics* 99, 69–83. doi:10.1016/j.intermet.2018.05.013

Liu, H., Feng, Y., Yao, Y., Li, B., Wang, R., Shi, X., et al. (2021). Effect of the 345°C and 16.5 MPa autoclave corrosion on the oxidation behavior of Cr-coated zirconium claddings in the high-temperature steam. *Corros. Sci.* 189, 109608. doi:10.1016/j.corsci.2021.109608

Long, Y., Zhang, G., Chen, J., Datye, A., Zhang, S., Schwarz, U. D., et al. (2023). Effect of yttrium on phase composition and microstructure of FeCoNiAlCrB high entropy alloys. *Mater. Sci. Eng. A* 873, 145058. doi:10.1016/j.msea.2023.145058

McCormack, S. J., and Navrotsky, A. (2021). Thermodynamics of high entropy oxides. *Acta Mater.* 202, 1–21. doi:10.1016/j.actamat.2020.10.043

McKamey, C. G., George, E. P., Liu, C. T., Horton, J. A., Carmichael, C. A., Kennedy, R. L., et al. (2000). *Manufacturing of nickel-base superalloys with improved high-temperature performance (No. C/ORNL95-0327)*. Oak Ridge, TN: Oak Ridge National Lab. (US).

Migas, D., Chmiela, B., Myalska-Głowacka, H., Moskal, G., Matus, K., and Swadźba, R. (2022). The effect of yttrium on oxide scale growth on Co-Al-W-based superalloys. *Corros. Sci.* 208, 110674. doi:10.1016/j.corsci.2022.110674

Miyazaki, N. (2016). Solid particle erosion of composite materials: a critical review. *J. Compos. Mater.* 50 (23), 3175–3217. doi:10.1177/0021998315617818

Nair, R. B., Ngan, S., and McDonald, A. (2023). Dry abrasive wear and solid particle erosion assessments of high entropy alloy coatings fabricated by cold spraying. *Mater. Today Commun.* 34, 105527. doi:10.1016/j.mtcomm.2023.105527

Naveed, M., Schlag, H., König, F., and Weiß, S. (2017). Influence of the erodent shape on the erosion behavior of ductile and brittle materials. *Tribol. Lett.* 65 (1), 18. doi:10.1007/s11249-016-0800-x

Qian, X. Y., Zeng, Y., Jiang, B., Yang, Q. R., Wan, Y. J., Quan, G. F., et al. (2020). Grain refinement mechanism and improved mechanical properties in Mg–Sn alloy with trace Y addition. *J. Alloys Compd.* 820, 153122. doi:10.1016/j.jallcom.2019.153122

Qiao, L., and Zhu, J. (2022). Microstructure, mechanical property and wear behavior of AlCrFe1.5Ni1.5 medium entropy alloy. *J. Mater. Sci.* 57 (26), 12629–12641. doi:10.1007/s10853-022-07416-0

Radu, I., and Li, D. Y. (2007). The wear performance of yttrium-modified Stellite 712 at elevated temperatures. *Tribol. Int.* 40 (2), 254–265. doi:10.1016/j.triboint.2005.09.027

Radu, I., and Li, D. Y. (2008). A further study of the beneficial effects of yttrium on oxide scale properties and high-temperature wear of stellite 21. *Tribol. Lett.* 30, 27–34. doi:10.1007/s11249-008-9308-3

Ramanarayanan, T. A., Ayer, R., Petkovic-Luton, R., and Leta, D. P. (1988). The influence of yttrium on oxide scale growth and adherence. *Oxid. Metals* 29, 445–472. doi:10.1007/bf00666845

Ren, H., Chen, R. R., Gao, X. F., Liu, T., Qin, G., Wu, S. P., et al. (2022). Insights on mechanical properties of dual-phase high entropy alloys via Y introduction. *J. Alloys Compd.* 929, 167374. doi:10.1016/j.jallcom.2022.167374

Ren, H., Chen, R. R., Liu, T., Gao, X. F., Qin, G., Wu, S. P., et al. (2024). Unraveling the oxidation mechanism of Y-doped AlCoCrFeNi high-entropy alloy at 1100°C. *Appl. Surf. Sci.* 652, 159316. doi:10.1016/j.apsusc.2024.159316

Rovere, F., Mayrhofer, P. H., Reinholdt, A., Mayer, J., and Schneider, J. M. (2008). The effect of yttrium incorporation on the oxidation resistance of Cr–Al–N coatings. *Surf. Coatings Technol.* 202 (24), 5870–5875. doi:10.1016/j.surfcoat.2008.06.161

Shi, H., Fetzer, R., Jianu, A., Weisenburger, A., Heinzel, A., Lang, F., et al. (2021). Influence of alloying elements (Cu, Ti, Nb) on the microstructure and corrosion behaviour of AlCrFeNi-based high entropy alloys exposed to oxygen-containing molten Pb. *Corros. Sci.* 190, 109659. doi:10.1016/j.corsci.2021.109659

Stoyanov, P., Dawag, L., Goberman, D. G., and Shah, D. (2018). Friction and wear characteristics of single crystal Ni-based superalloys at elevated temperatures. *Tribol. Lett.* 66, 47–49. doi:10.1007/s11249-018-0994-1

Tang, Y., and Li, D. Y. (2021). Nano-tribological behavior of high-entropy alloys CrMnFeCoNi and CrFeCoNi under different conditions: a molecular dynamics study. *Wear* 476, 203583. doi:10.1016/j.wear.2020.203583

Tsai, M. H., and Yeh, J. W. (2014). High-entropy alloys: a critical review. *Mater. Res. Lett.* 2 (3), 107–123. doi:10.1080/21663831.2014.912690

Wang, G., Liu, H., Tao, X., Zhou, S., Li, J., Zou, H., et al. (2024). Unraveling the plastic deformation, recrystallization, and oxidation behavior of Waspaloy during thermal fatigue crack propagation. *J. Alloys Compd.* 1004, 175814. doi:10.1016/j.jallcom.2024.175814

Whittle, D. P., and Stringer, J. (1980). Improvements in high temperature oxidation resistance by additions of reactive elements or oxide dispersions. *Philosophical Trans. R. Soc. Lond. Ser. A, Math. Phys. Sci.* 295 (1413), 309–329. doi:10.1098/rsta.1980.0124

Wu, M., Sim, R. K., He, A., Diao, G., Chen, W., Chen, D., et al. (2023). Mechanisms underlying the influence of Co and Ti on the microstructure, mechanical and wear properties of A2/B2 typed AlCrFeNi alloy. *J. Alloys Compd.* 968, 172070. doi:10.1016/j.jallcom.2023.172070

Wu, Y., and Hwang, S. K. (2002). Microstructural refinement and improvement of mechanical properties and oxidation resistance in EPM TiAl-based intermetallics with yttrium addition. *Acta mater.* 50 (6), 1479–1493. doi:10.1016/s1359-6454(02)00006-x

Wu, Y., Li, Y., Xu, Y., Kang, M., Wang, J., and Sun, B. (2021). Unveiling the mechanism of yttrium-related microstructure inhibiting or promoting high-temperature oxidation based on Ni-Al-Y alloys. *Acta Mater.* 211, 116879. doi:10.1016/j.actamat.2021.116879

Xu, X. D., Liu, P., Guo, S., Hirata, A., Fujita, T., Nieh, T. G., et al. (2015). Nanoscale phase separation in a fcc-based CoCrCuFeNiAl0. 5 high-entropy alloy. *Acta Mater.* 84, 145–152. doi:10.1016/j.actamat.2014.10.033

Xu, Z., He, A. Q., Tang, Y. Q., Chen, K. Y., Diao, G. J., Wu, M. Y., et al. (2025). Solid-particle erosion resistance of NbC-reinforced AlCrFeNi medium-entropy alloy at ambient and elevated temperatures. *Wear*, 205950. doi:10.1016/j.wear.2025.205950

Xu, Z., Li, D. Y., Diao, G., Wu, M. Y., Fraser, D., Li, J., et al. (2024b). Effects of NbC addition on mechanical and tribological properties of AlCrFeNi medium-entropy alloy. *Tribol. Int.* 194, 109486. doi:10.1016/j.triboint.2024.109486

Xu, Z., Tang, Y. Q., He, A. Q., Chen, W. G., Chen, D. L., and Li, D. Y. (2024a). Opposite bauschinger effects on wear of high-entropy alloy AlCoCrFeNi x (x= 0 to 2) under sliding wear and machining conditions. *Metallurgical Mater. Trans. A* 55 (6), 2098–2115. doi:10.1007/s11661-024-07382-z

Ye, H. Z., Liu, R., Li, D. Y., Eadie, R., and Li, D. (1999). Development of a new wear-resistant material: TiC/TiNi composite. *Scr. Mater.* 41, 1039–1045. doi:10.1016/s1359-6462(99)00236-5

Yeh, J. W. (2006). Recent progress in high entropy alloys. *Ann. Chim. Sci. Mat.* 31 (6), 633–648. doi:10.3166/acsm.31.633-648

Yi, X., Sun, K., Wang, H., Gong, Y., Meng, X., Gao, Z., et al. (2021). Tuning microstructure, transformation behavior, mechanical/functional properties of Ti–V–Al shape memory alloy by doping quaternary rare earth Y. *Prog. Nat. Sci. Mater. Int.* 31 (2), 296–302. doi:10.1016/j.pnsc.2020.12.012

Zhang, L. J., Zhang, M. D., Zhou, Z., Fan, J. T., Cui, P., Yu, P. F., et al. (2018). Effects of rare-earth element, Y, additions on the microstructure and mechanical properties of CoCrFeNi high entropy alloy. *Mater. Sci. Eng. A* 725, 437–446. doi:10.1016/j.msea.2018.04.058

Zhang, S., Han, B., Li, M., Zhang, Q., Hu, C., Niu, S., et al. (2021). Investigation on solid particles erosion resistance of laser cladded CoCrFeNiTi high entropy alloy coating. *Intermetallics* 131, 107111. doi:10.1016/j.intermet.2021.107111

Zhang, S., Han, B., Zhang, T., Chen, Y., Xie, J., Shen, Y., et al. (2023). High-temperature solid particle erosion characteristics and damage mechanism of AlxCoCrFeNiSi high-entropy alloy coatings prepared by laser cladding. *Intermetallics* 159, 107939. doi:10.1016/j.intermet.2023.107939

Zhang, S., Li, H., Jiang, Z., Feng, H., Wen, Z., Ren, J., et al. (2022). Unveiling the mechanism of yttrium significantly improving high-temperature oxidation resistance of super-austenitic stainless steel S32654. *J. Mater. Sci. and Technol.* 115, 103–114. doi:10.1016/j.jmst.2022.01.001

Zhang, Y., Zuo, T. T., Tang, Z., Gao, M. C., Dahmen, K. A., Liaw, P. K., et al. (2014). Microstructures and properties of high-entropy alloys. *Prog. Mater. Sci.* 61, 1–93. doi:10.1016/j.pmatsci.2013.10.001

Zhou, H., Mao, J., Jiang, H., Zhang, H., Wei, W., Qin, S., et al. (2023). Effect of rare-earth element Y addition on microstructure and mechanical properties of CrFeNi2 medium entropy alloy. *Intermetallics* 163, 108079. doi:10.1016/j.intermet.2023.108079

Zhou, S., Shu, X., Hu, L., Yuan, X., Qiu, P., and Xu, X. (2025). Effects of Y Additions on the microstructure and mechanical properties of CoCr1.7Ni medium-entropy alloys. *Crystals* 15 (2), 172. doi:10.3390/cryst15020172